PAPER

Check for updates

Core–shell nanoparticles with tensile strain enable highly efficient electrochemical ethanol oxidation†

Moxuan Liu,‡[a] Miao Xie,‡[b] Yilan Jiang, [ID][c] Zhaojun Liu,[a] Yiming Lu,[b] Shumeng Zhang,[a] Zhixue Zhang,[a] Xiaoxiao Wang,[a] Kai Liu,[a] Qing Zhang,[c] Tao Cheng [ID] *[b] and Chuanbo Gao [ID] *[a]

The ethanol oxidation reaction (EOR), the anode reaction of direct ethanol fuel cells, suffers from sluggish oxidation kinetics and low selectivity toward complete oxidation to CO_2. The key to solving the above problems is to design and synthesize high-performance catalysts. In this work, we synthesize Ag@AgPd core–shell nanoparticles that exhibit a significant improvement in catalytic performance. Specifically, in 1.0 M KOH + 1.0 M EtOH, the mass activity of the Ag@AgPd core–shell catalyst reaches up to 12.7 A mg_{Pd}^{-1} with a significantly improved selectivity toward CO_2 by 4.5 times compared with commercial Pd/C. This superior performance guarantees that this Ag@AgPd core–shell nanoparticle is among the best-reported catalysts. Mechanism study by density functional theory shows that the tensile strain that originates from the unique core–shell structure decreases the potential determining step by 39%, which plays the most important role in increasing the activity and selectivity. This work demonstrates the effect of the tensile strain in promoting the kinetics and selectivity of the EOR, which may serve as a guide for the design of highly efficient electrocatalysts for general alcohol oxidation reactions by controlled nanoparticle synthesis.

Introduction

Direct ethanol fuel cells (DEFCs) are promising energy conversion devices potentially applicable to the power supply of mobile electronics and vehicles.[1–3] As a fuel, ethanol is preferable over methanol, a prevalent fuel of current research interest, because it is non-toxic, less reactive, and thus greener, has a higher energy density, and can be produced from biomass fermentation in large amounts without relying on fossil resources.[3,4] However, the ethanol oxidation reaction (EOR) is a sluggish process. It requires a large overpotential to attain a specific current density, which is a bottleneck of the technology toward practical applications. Moreover, ethanol is usually partially oxidized without the cleavage of the C–C bond,

delivering only 2 and 4 electrons per molecule to afford acetaldehyde and acetate, respectively ("C2 path").[5–15] Compared with the complete oxidation of ethanol that delivers 12 electrons per molecule to produce CO_2 ("C1 path"), the energy conversion efficiency of the EOR *via* the C2 path is drastically suppressed. For these reasons, great advances in reducing the energy barriers in the reaction pathway of the EOR and improving the C1-path selectivity against the C2 path are highly demanded prior to the mass application of DEFCs.

Nanoparticles of noble metals such as Pd and Pt, and their alloys are recognized as excellent choices of catalysts for the EOR.[16] Because of the complexity of intermediates involved in ethanol oxidation and the difficulty in gaining a full understanding of the reaction mechanisms, it has been difficult to achieve high catalytic activity and C1-path selectivity with these noble metal catalysts. Current studies show that it is difficult to oxidize ethanol to CO_2 or carbonate on Pd or Pt-based catalysts, with the main product being acetate.[5,8,17–19] Sun *et al.* revealed by *in situ* infrared spectroscopy that the faradaic efficiency (FE) of the C1 path is less than 2.5% on Pd-based catalysts.[8] Zhu *et al.* also indicated that the selectivity of the C1 path is less than 5% on Pd.[5] To some extent, this problem can be alleviated by introducing Rh or Ir into the catalyst.[10–12] These metals are considered to promote the cleavage of the C–C bond in ethanol, which contributes to improved C1-path selectivity and hence the overall activity. Moreover, low-coordination metal sites[13] and metal/SnO_2 interfaces are also found to be favorable for

[a]*Center for Materials Chemistry, Frontier Institute of Science and Technology and State Key Laboratory of Multiphase Flow in Power Engineering, Xi'an Jiaotong University, Xi'an, Shaanxi 710054, China. E-mail: gaochuanbo@mail.xjtu.edu.cn*

[b]*Institute of Functional Nano & Soft Materials (FUNSOM), Jiangsu Key Laboratory for Carbon-Based Functional Materials & Devices, Joint International Research Laboratory of Carbon-Based Functional Materials and Devices, Soochow University, Suzhou, Jiangsu 215123, China. E-mail: tcheng@suda.edu.cn*

[c]*Center for High-resolution Electron Microscopy (ChEM), School of Physical Science and Technology, ShanghaiTech University, Shanghai 201210, China*

† Electronic supplementary information (ESI) available: Full experimental details, DFT modeling, additional UV-vis spectra, XRD patterns, XPS spectra, TEM images, electrocatalysis data, and a survey of alcohol oxidation catalysts in the literature. See DOI: 10.1039/d1ta03365d

‡ M. L. and M. X. contributed equally to this work.

This journal is © The Royal Society of Chemistry 2021

J. Mater. Chem. A, 2021, **9**, 15373–15380 | **15373**

selective ethanol oxidation *via* the C1 path.[14,15] Despite these endeavors, there are very few mechanisms that have been verified to be effective in tuning the selectivity and activity of the EOR, to the best of our knowledge, which impedes the rational design of high-performance noble metal catalysts for this reaction.

Herein, we report the unambiguous efficacy of strong tensile strains in a Pd catalyst in improving both the reaction kinetics and the C1-path selectivity in the EOR. The tensile strain was generated by the galvanic-replacement-free epitaxial growth of Pd on Ag templates, forming a core–shell nanostructure (denoted as Ag@AgPd, due to the interfacial alloying). The Pd atoms in the shell are found to take precisely the same arrangement as the Ag atoms in the core, leading to a substantial expansion of the lattice size by 4.5%. Experiments and density functional theory (DFT) calculations show that the tensile strain significantly increases the strength of the interaction between the catalyst and the intermediates involved in the EOR, leading to a substantial decrease in the energy barrier associated with the dehydration of ethanol *via* the C2 path by 39%, relative to the unstrained monometallic Pd/C. Although the C2 path dominates in the EOR, the tensile strain significantly diminishes the energy barrier difference between the C1 and the C2 paths, which accounts for the remarkable C1-path faradaic efficiency with the Ag@AgPd core–shell catalysts (FE, 18%), 4.5 times greater than that of unstrained Pd/C (FE, ~4%). As a result, the Ag@AgPd core–shell catalysts demonstrated a mass activity of 12.7 A mg_{Pd}^{-1} in the EOR under alkaline conditions, 12.8 times greater than that of commercial Pd/C, which places it in a leading position among all Pd-based catalysts reported to date. Our results reveal the effect of the tensile strain on the kinetics and selectivity of the ethanol oxidation reaction, which opens new opportunities to design highly efficient noble metal catalysts for the oxidation of ethanol and a broader range of biomass-derived alcohols for fuel cell applications.

Results and discussion

Synthesis and characterization

A core–shell structure represents an ideal platform for strain engineering of noble metal catalysts.[20–24] Considerable strains could be formed in the Pd shells when metals of different lattice sizes are selected as the cores (or "templates"). Another benefit of the core–shell structure is the reduced cost of the catalyst when a less precious metal is used as the template. To this end, we chose Ag nanoplates as the templates because Ag possesses a much larger lattice size and a much lower price than Pd, which enables us to generate strong tensile strains in Pd at a low cost. The synthesis of the Ag@Pd core–shell structure, however, remains a significant challenge. A galvanic replacement reaction readily occurs between the Ag templates and the Pd salt, leading to the excavation of the nanostructure, accelerated Ag–Pd alloying. Therefore a loss of control over the structure and composition of the catalyst occurs.[25,26] Although Ag@Pd core–shell nanocrystals have been of interest in recent years,[14,27–34] reliable suppression of the galvanic replacement reaction has been rarely achieved, especially from an aqueous system that

usually produces easily processable nanocrystals with a clean surface.[27] Inspired by our previous work,[35–38] we here introduce glucose as a ligand to lower the reduction potential of the Pd salt and hence its tendency to participate in the galvanic replacement reaction with the Ag nanoplates. Upon mixing glucose with NaPdCl4, the solution showed a gradual increase in the ultraviolet-visible (UV-vis) absorbance, displaying a yellow color that deepened with time, which is a clear sign of the formation of a stable coordination compound (Fig. S3†). Further stabilization of the Ag nanoplates was conducted by adsorbing diethylamine onto their surface.[38,39] As a result, the galvanic replacement reaction has been successfully circumvented, making it possible to grow Pd on the Ag nanoplates in a highly controllable layer-by-layer manner.

The core–shell nanoplates obtained from this synthesis are denoted as Ag@AgPd$_{n\mathrm{L}}$, where nL is the estimated number of the atomic layers of Pd on the Ag (111) surface according to the Pd/Ag ratio, assuming that the shell is composed of Pd which is uniformly deposited on the Ag surface (Fig. S2 and Table S2†). Fig. S4† shows a typical transmission electron microscopy (TEM) image of the Ag@AgPd$_{3.6\mathrm{L}}$ core–shell nanoplates (shell thickness, ~0.8 nm on basal (111) facets). No obvious cavities or pinholes can be observed on the nanoplates, confirming the absence of the galvanic replacement reaction in this synthesis. For comparison, significant hollowing of the Ag nanoplates occurred when either glucose or diethylamine was absent in the synthesis, highlighting their critical roles in suppressing the galvanic replacement reaction (Fig. S5†). Although it is difficult to distinguish the core–shell boundary by TEM imaging, due to the close atomic numbers of the metals, the energy-dispersive X-ray spectroscopy (EDS) elemental mapping (Fig. 1a) and the line scan of an Ag@AgPd$_{3.6\mathrm{L}}$ core–shell nanoplate (Fig. 1b) clearly show the presence of an ultrathin layer of Pd on the surface of the Ag nanoplates. Driven by the significant gap in the surface energy of the metals (Ag: 1.25 J m^{-2}; Pd: 2.05 J m^{-2}), outward diffusion of Ag through the Pd shell inevitably occurs during the crystal growth.[40] A depth-dependent X-ray photoelectron spectroscopy (XPS) analysis indicates enhanced Ag–Pd alloying as the detecting depth approaches the Ag/Pd interface (Fig. 1c). Cyclic voltammetry (CV) confirms a decrease in the coverage of Ag with increasing shell thickness (Fig. S6†). Because the galvanic replacement reaction was eliminated in the synthesis, the Ag–Pd alloying in the epitaxial layer has already been suppressed to a great extent. The highly suppressed while controllable Ag–Pd alloying in the shells may introduce an additional ligand effect that collaborates with the strains to achieve distinctive catalytic properties.

To reveal the atomic arrangements of Pd on the Ag nanoplates, we examined the crystal structure of the Ag@AgPd$_{3.6\mathrm{L}}$ core–shell nanoplates by spherical-aberration-corrected high-resolution TEM (HRTEM) under a high-angle annular dark-field scanning transmission electron microscopy (HAADF-STEM) mode (Fig. 1d). This image was taken at a long edge of the truncated triangular nanoplate. The dashed line indicates the approximate core–shell boundary, assuming a uniform shell thickness of 0.8 nm. The (220) lattice fringes with a spacing of ~1.45 Å extend from the center to the edge of the nanoplate
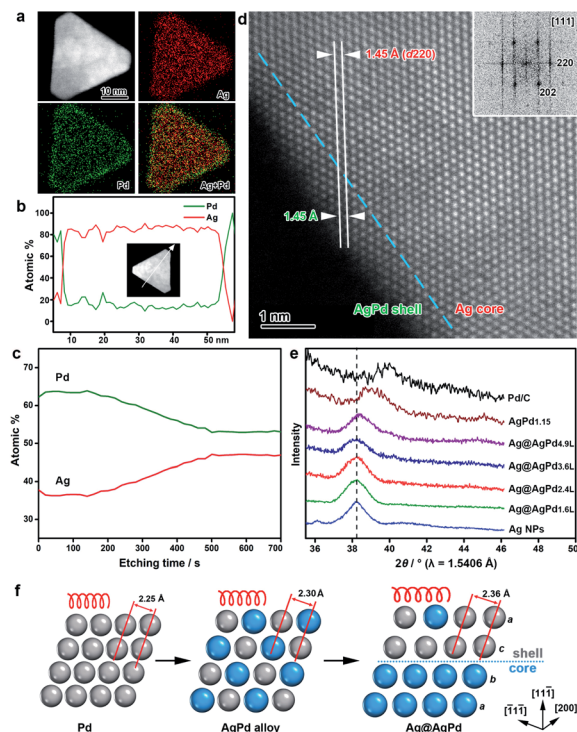
Fig. 1 Characterization of the Ag@AgPd core−shell nanoplates. (a and b) EDS elemental mapping and a line scan of an Ag@AgPd$_{3.6L}$ core−shell nanoplate. (c) Depth-dependent elemental analysis of the core−shell nanoplates by XPS with a continuous etching of the nanoplates with Ar$^+$. (d) High-resolution HAADF-STEM image of an Ag@AgPd$_{3.6L}$ core−shell nanoplate. The dashed line indicates the approximate core−shell boundary. (Inset) A Fourier diffractogram. (e) XRD patterns of the Ag@AgPd$_{nL}$ core−shell nanoplates, AgPd$_{1.15}$ alloy nanoparticles, Ag nanoplates, and Pd/C. The dashed line indicates the position of the 111 reflections from Ag. (f) A scheme showing the lattice size expansion in the order of Pd < Ag−Pd alloy < Ag@AgPd core−shell nanostructure.

without variations in the d-spacing, which confirms obvious core−shell epitaxy: the lattice size of the AgPd shell is solely determined by the Ag core and expands substantially from its intrinsic value, generating intense tensile strains. We further investigated the tensile strains in a series of Ag@AgPd$_{nL}$ core−shell nanoplates on a whole-sample basis by X-ray diffraction (XRD), compared with monometallic Ag (Ag nanoplates), Pd (commercial Pd/C), and AgPd$_{1.15}$ alloy nanoparticles (Fig. 1e and S7−S9†). Here, $n = 1.6$, 2.4, 3.6, and 4.9, corresponding to the epitaxial layer thickness of ∼0.4, 0.6, 0.8, and 1.2 nm, respectively, on the basal (111) faces. The Ag@AgPd$_{nL}$ ($n = 1.6$, 2.4, and 3.6) core−shell nanoplates display 111 reflections simultaneously as that of the Ag nanoplates. A slight shift of the X-ray reflection to a higher 2θ can be observed when the shell becomes too thick ($n = 4.9$). For comparison, the 111 reflections of the AgPd$_{1.15}$ alloy nanoparticles are located well between those of monometallic Ag and Pd. Therefore, the lattice size increases in the order of Pd < Ag−Pd alloy < Ag@AgPd core−shell nanoplates ≈ Ag nanoplates. The lattice sizes of the Ag−Pd alloy and Pd nanoparticles can also be characterized by HRTEM imaging (Fig. S10 and S11†). The core−shell structure expands the lattice size of Pd to a much larger extent than its alloy counterpart (Fig. 1f).

Electrochemical performance

The catalytic activities of the Ag@AgPd$_{nL}$ core−shell nanoplates in the EOR (1 M KOH + 1 M EtOH) were investigated and compared with those of the AgPd$_{1.15}$ alloy nanoparticles and commercial Pd/C (Fig. 2). Based on the integrated charge associated with the PdO reduction, the electrochemically active surface areas (ECSAs) of the Ag@AgPd$_{nL}$ core−shell nanoplates (supported on carbon, Fig. S12†) are estimated to be 80.5 ($n = 1.6$), 72.5 ($n = 2.4$), 69.3 ($n = 3.6$), and 36.4 m^2 g$_{Pd}^{-1}$ ($n = 4.9$), which are higher than that of commercial Pd/C (35.4 m^2 g$_{Pd}^{-1}$) (Fig. S13†). These core−shell nanoplates show excellent ethanol oxidation activities, superior to commercial Pd/C, and more notably, to the AgPd$_{1.15}$ alloy nanoparticles (Fig. 2a, b, S14 and S15†). Interestingly, the catalytic activity of the Ag@AgPd core−shell nanoplates depends on the shell thickness. With increasing shell thickness, the catalytic activity increases and decreases, reaching an optimal value with the Ag@AgPd$_{3.6L}$ catalyst (mass activity: 12.7 A mg$_{Pd}^{-1}$; specific activity: 18.2 mA cm^{-2}; mean values of three parallel experiments (Table S3†)). Compared with Pd/C and the AgPd$_{1.15}$ alloy nanoparticles, the Ag@AgPd$_{3.6L}$ catalyst shows an increase in the mass activity by a factor of 12.8 and 14.0 and an increase in the specific activity by a factor of 6.5 and 2.5, respectively, highlighting the critical role of the Ag@AgPd core−shell structure in gaining exceptional ethanol oxidation activity. The catalytic activity of the Ag@AgPd$_{3.6L}$ core−shell nanoplates substantially exceeds those of most Pd-based catalysts reported to date, making them a top-ranked catalyst for this reaction to the best of our knowledge (Table S4†).[4,11,13,41–45]
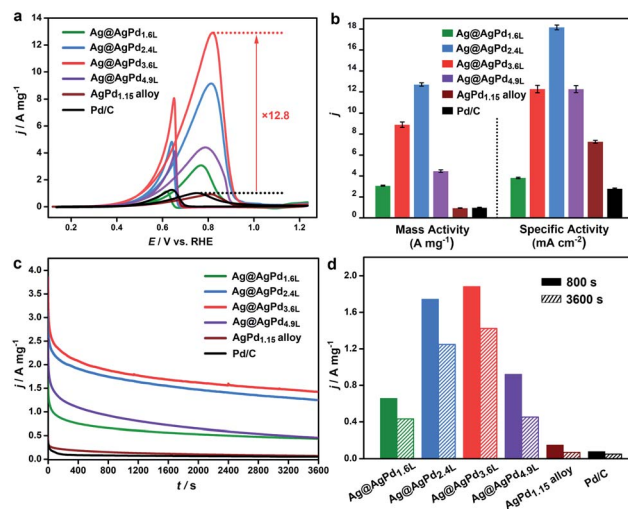
Fig. 2 Performance of the Ag@AgPd core−shell nanoplates, the AgPd$_{1.15}$ alloy nanoparticles, and commercial Pd/C in the electro-catalytic EOR. (a) CV curves of the catalysts in N$_2$-saturated 1 M KOH + 1 M EtOH at a scan rate of 50 mV s^{-1}. (b) Specific and mass activities of the catalysts in terms of the anodic peak currents normalized to the mass of Pd and the ECSA, respectively. The specific and mass activities were measured independently with 3 parallel samples, with the error bars indicating the standard deviations. (c) The i–t curves of the catalysts at 0.635 V $vs.$ RHE. (d) Comparison of the currents at 800 s and 3600 s during the i–t analysis of the catalysts.

The Ag@AgPd core–shell nanoplates also show improved catalytic durability compared with the Ag–Pd alloy nanoparticles and commercial Pd/C (Fig. 2c and d). In an i–t measurement at 0.635 V, the activities of the $AgPd_{1.15}$ alloy nanoparticles and commercial Pd/C decreased rapidly. In contrast, the Ag@AgPd core–shell nanoplates retained most of their initial activities. After 1 h, the mass activity of the $Ag@AgPd_{3.6L}$ core–shell nanoplates (1.423 A mg_{Pd}^{-1}) was 20.6 and 27.8 times higher than those of the $AgPd_{1.15}$ alloy nanoparticles (0.069 A mg_{Pd}^{-1}) and Pd/C (0.051 A mg_{Pd}^{-1}), respectively. The high catalytic durability of the core–shell catalysts can be attributed to the improved CO tolerance (discussed later) and the structural and compositional stability during the electrocatalysis (Fig. S16 and Table S5†).

Besides ethanol, the Ag@AgPd core–shell nanoplates show remarkable activity in the oxidation of many other biomass-derived alcohols (Fig. S17, S18 and Tables S6 and S7†). Mass activities of 10.2 and 6.63 A mg^{-1} have been achieved in the oxidation of ethylene glycol (0.5 M KOH + 0.5 M ethylene glycol) and glycerol (1 M KOH + 0.1 M glycerol), 6.3 and 8.0 times greater than those of commercial Pd/C, respectively, validating the efficacy of the tensile strain in accelerating the oxidation kinetics of a broad range of alcohols.
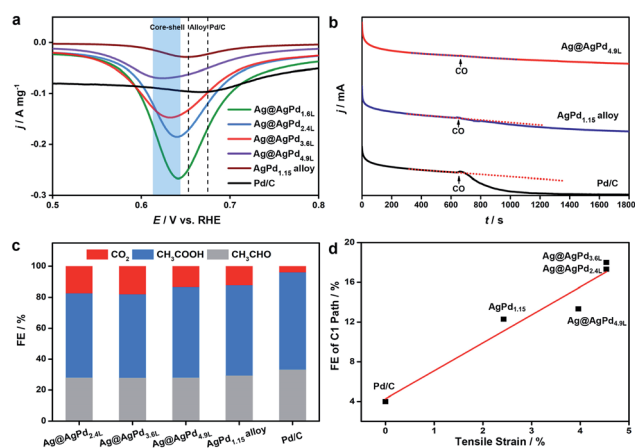
Mechanisms

To disclose the mechanism for the boosted ethanol oxidation kinetics with the Ag@AgPd core–shell nanoplates, we investigated experimentally the adsorption energy of *OH as a measure of the interaction between the catalyst and ethanol

Fig. 3 Effects of the tensile strains. (a) Comparison of the PdO reduction peaks on different catalysts. The dashed lines and the color zone indicate the peak positions of Pd/C, the $AgPd_{1.15}$ alloy nanoparticles, and the Ag@AgPd core–shell nanoplates. (b) Chronoamperometric i–t curves of the catalysts at 0.635 V $vs.$ RHE in N_2-saturated 1 M KOH + 1 M EtOH; the gas was switched from N_2 to CO at ~650 s. Dashed lines indicate the slopes of the current density curves at the point of CO bubbling. (c) Faradaic efficiencies of the C1- and C2-path products with the catalysts of the $Ag@AgPd_{nL}$ core–shell nanoplates, the $AgPd_{1.15}$ alloy nanoparticles, and Pd/C in N_2-saturated 0.1 M KOH + 1 M EtOH at 0.635 V $vs.$ RHE with the same electricity (50 C). (d) The linear relationship between the lattice strain and the C1-path faradaic efficiency of the EOR.

and therefore the ability of the catalyst to activate ethanol (Fig. 3a).[45–47] In a typical electrocatalytic CV measurement, the PdO reduction peaks undergo an obvious cathodic shift in the order of Pd/C (~0.68 V) > $AgPd_{1.15}$ alloy nanoparticles (~0.65 V) > $Ag@AgPd_{nL}$ core–shell nanoplates (0.62–0.64 V), suggesting significantly increased adsorption energy of *OH in this order, which can be attributed to increasing tensile strains in the AgPd shells and thus the higher position of the d-band center.[48–50] The Ag@AgPd core–shell nanoplates show the highest adsorption energy of *OH and thus the highest ability to activate ethanol and its intermediates, in line with their exceptional catalytic activities in the EOR. It is worth noting that the adsorption energy of *OH varies with the shell thickness, despite similar strength of the tensile strains. With decreasing shell thickness from 4.9 to 1.6 layers, the PdO reduction potentials shift from 0.62 to 0.64 V, which can be attributed to the thickness-dependent Ag–Pd alloying and the Ag–Pd electron transfer in the shells (Fig. S19†). It suggests that the Ag–Pd electron transfer weakens the adsorption energy of *OH unfavorably. Therefore, a sufficient shell thickness is required to obtain an optimum ethanol oxidation activity ($Ag@AgPd_{3.6L}$). A further increase in the shell thickness leads to a decrease in the tensile strain (Fig. 1e), which accounts for the drop in the catalytic activity.

The Ag–Pd electron transfer helps overcome the poisoning of the catalyst by *CO, an intermediate possibly produced via the C1-path ethanol oxidation. To verify it, we examined the change in the current density when CO is bubbled into the electrolyte (1 M KOH + 1 M EtOH) during a chronoamperometric i–t analysis (Fig. 3b; CO stripping, Fig. S20 and S21†). Commercial Pd/C showed an abrupt current drop due to the strong adsorption of CO on the catalyst. In contrast, the current drop with the $AgPd_{1.15}$ alloy nanoparticles was less prominent, and that with the $Ag@AgPd_{4.9L}$ core–shell nanoplates became indiscernible. This observation verifies the role of the Ag–Pd electron transfer in weakening the adsorption energy of *CO, which can be attributed to the decreased d vacancy in Pd and thus weakened Pd–CO bond strength. Therefore, the CO intermediate produced in the EOR could be rapidly removed from the Ag@AgPd surface, contributing to enhanced catalytic activity and durability in the EOR.

The C–C bond cleavage of ethanol contributes to the energy conversion efficiency and the overall current density of the EOR. Previous studies indicate that the main product of the EOR on Pd-based catalysts in alkaline medium is acetate,[5,8,17–19] and the C1-path selectivity is usually less than 2.5% or 5%.[5,8] To evaluate the C1-path selectivity of our catalysts, we analyzed the final products in the electrolytes by high-performance liquid chromatography (HPLC) (Fig. 3c). Experimentally, the EOR proceeded at a constant potential of 0.635 V in N_2-saturated 0.1 M KOH + 1 M EtOH and stopped when the quantity of electricity reached 50 C. HPLC measured the concentrations of CH_3COOH and CH_3CHO to obtain the faradaic efficiency (FE) of the C2-path reaction (ESI†). The FE of the C1-path reaction to produce CO_2 was calculated by subtracting the C2-path FE from 100% FE, assuming no side reactions (Fig. S22†). The FEs of the C1-path reaction were determined to be 17.3% ($Ag@AgPd_{2.4L}$),

15376 | J. Mater. Chem. A, 2021, 9, 15373–15380

This journal is © The Royal Society of Chemistry 2021

18.0% (Ag@AgPd$_{3.6L}$), 13.5% (Ag@AgPd$_{4.9L}$), 13.3% (AgPd$_{1.15}$), and 4.0% (Pd/C, consistent with literature reports[5,8]). Therefore, The FEs of the C1-path reaction increase in the order of Pd < Ag–Pd alloy < Ag@AgPd. The AgPd$_{1.15}$ alloy nanoparticles already showed significantly higher C1-path FE than Pd/C. Here, the contributions from the ligand and strain effects cannot be disentangled in this alloy system. However, when we plotted all the C1-path FE values against the tensile strains (defined as $(d_{111,\text{catalyst}} - d_{111,\text{Pd}})/d_{111,\text{Pd}}$, with d-spacing values extracted from the XRD data)[23] in all Pd catalysts investigated, we found a roughly linear relationship, which indicates a direct correlation between the C1-path selectivity and the tensile strains in the Pd-based catalysts (Fig. 3d). The Ag@AgPd$_{3.6L}$ core–shell nanoplates demonstrated the highest C1-path FE, which was 4.5 times greater than that of commercial Pd/C, contributing to their exceptional catalytic activity in the EOR.

We carried out DFT calculations to understand the effect of the tensile strain in the Ag@AgPd core–shell nanostructure on the catalytic activity and C1-path selectivity of the EOR (Fig. 4). The binding energies of *OH and *CO are widely employed as descriptors of alcohol oxidation reactions to represent the complex reaction network. It is accepted that catalysts with facile *OH generation and high *CO tolerance will have improved catalytic efficacies for the EOR, which requires stronger *OH binding energy and weaker *CO binding energy. First, we calculated the adsorption energies of *OH and *CO, two critical descriptors for alcohol oxidation reactions (Fig. 4b).[45–47,51] Compared with Pd (111), all Ag–Pd alloy (111) surfaces (Ag/Pd: 3 : 1–1 : 3; lattice size following that of Ag to mimic the Ag@AgPd surface) show significantly increased adsorption energies of *OH, due to the exceptional tensile

strains, suggesting their high ability to activate ethanol and its intermediates. Both the adsorption energies of *OH and *CO decrease with the Ag/Pd ratios, confirming the significant Ag–Pd ligand effect. These findings align well with experimental observations (Fig. 3a and b) and affirm the critical role of the Ag@AgPd core–shell configuration in improving the ethanol oxidation kinetics.

Then, we evaluated the possible energy evolutions of the C1- and C2-path EOR on the surface of various catalysts (Fig. 4c–e and S23†). Fig. 4a lists the reaction intermediates considered in this analysis.[6,13] A sequence of ethanol dehydrogenation occurs to form *CH$_3$CO, which is then converted through the C1 and C2 paths into *CO$_2$ and *CH$_3$COO$^-$, respectively. For all models investigated (Pd, Ag/Pd 1 : 1 alloy, and Ag@AgPd with an Ag/Pd 1 : 1 alloy shell), the dehydrogenation of ethanol is the rate-determining step of the EOR. With increasing tensile strain in the Pd catalyst, the energy barrier associated with the dehydrogenation reaction decreases dramatically. Specifically, this energy barrier is 0.92 eV (*CH$_3$CHOH → *CH$_3$COH) on a Pd surface, 0.86 eV (*CH$_3$CHOH → *CH$_3$COH) on an Ag–Pd alloy surface, and 0.76 eV (*CH$_3$CO → *CH$_2$CO, for C1 path) or 0.56 eV (*CH$_3$CH$_2$OH → *CH$_3$CHOH, for C2 path) on an Ag@AgPd core–shell surface. This result verifies the efficacy of the tensile strain in activating ethanol by accelerating its dehydrogenation for efficient oxidation. More accurate estimation of cleavage of the C–C bond also requires calculations of transition states, which will be considered in our future work. Considering the dominant C2-path selectivity, the energy barrier associated with the dehydrogenation of ethanol on the Ag@AgPd surface is lowered by 39% compared with that on the Pd surface, confirming the superiority of the Ag@AgPd core–shell structure in accelerating the ethanol oxidation kinetics.

The DFT calculation further validates the efficacy of the tensile strain in improving the C1-path selectivity of the EOR. From all models investigated, the energy barrier of the C1 path is higher than that of the C2 path, which is in line with the overwhelming C2-path selectivity of the EOR. With increasing tensile strains, the energy barrier in the *CH$_3$CO → *CO$_2$ branch of the reaction (C1 path) readily decreases (Pd: 0.85 eV; Ag–Pd alloy: 0.76 eV; Ag@AgPd: 0.76 eV), while that in the *CH$_3$CO → *CO$_2$ branch (C2 path) increases (Pd: 0.19 eV; Ag–Pd alloy: 0.23 eV; Ag@AgPd: 0.55 eV). As a result, the energy barrier difference between the C1 and the C2 paths diminishes in the order of Pd (0.66 eV) > Ag–Pd alloy (0.53 eV) > Ag@AgPd (0.21 eV), leading to improved C1-path selectivity in this order. This result, thus, confirms the critical role of the tensile strain in improving the C1-path selectivity and thus the energy conversion efficiency of the EOR.

Conclusions

Fig. 4 DFT calculation results. (a) Intermediates involved in the C1- and C2-path oxidation of ethanol. (b) Adsorption energies of *OH and *CO on different surfaces: Pd(111) and Pd–Ag(111) with the lattice size of Ag and different Ag/Pd ratios. (c–e) Reaction energy profiles of the intermediates involved in the C1- and C2-path EOR on Ag@AgPd (Ag/Pd = 1 : 1, d_{111}: 2.36 Å) (c), Ag–Pd alloy (Ag/Pd = 1 : 1, d_{111}: 2.30 Å) (d), and Pd (d_{111}: 2.25 Å) (e), respectively.

In summary, we have developed a galvanic-replacement-free strategy to synthesize Ag@AgPd core–shell nanoplates, and on this basis, revealed the unambiguous efficacy of the tensile strain in a Pd-based catalyst in addressing the current challenges of the electrocatalytic ethanol oxidation reaction, i.e., the sluggish dehydrogenation kinetics of ethanol and the low C1-
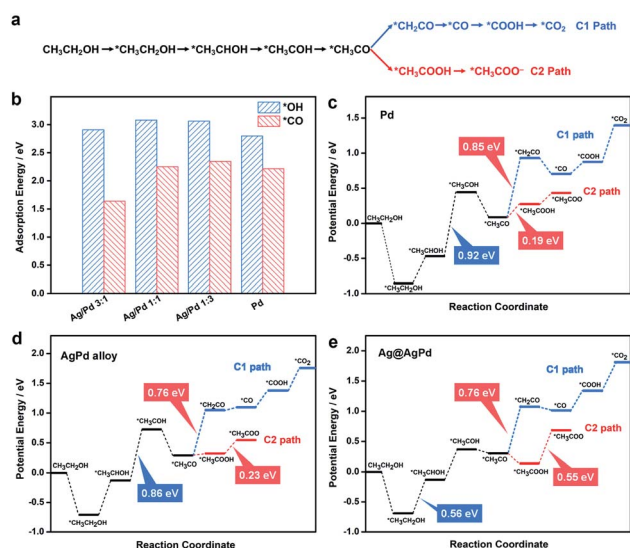
This journal is © The Royal Society of Chemistry 2021

J. Mater. Chem. A, 2021, **9**, 15373–15380 | **15377**

path selectivity. Owing to the core–shell epitaxy, the lattice size of Pd in the shell is expanded to a much greater extent than that of the Ag–Pd alloy counterpart, leading to increased interactions between ethanol and the catalyst and thus decreasing energy barriers associated with the dehydrogenation of ethanol, the rate-determining step of the dominant C2-path ethanol oxidation reaction. Besides, the tensile strain in the Pd catalyst substantially alters the selectivity of the ethanol oxidation reaction. The C1-path faradaic efficiencies of the catalysts increase in the order of Pd < Ag–Pd alloy < Ag@AgPd. DFT calculations show that the energy barrier of the C1 path significantly decreases. The energy barrier of the C2 path increases in this order, validating the direct connection between the C1-path selectivity and the tensile strain in the Pd catalyst. Both contribute to the exceptional catalytic activity of the Ag@AgPd core–shell catalyst in the EOR. Because Au possesses a similar lattice size to Ag, we expect that the Ag core could be facilely changed to Au, which may also exhibit high ethanol oxidation kinetics due to the strain effects. We believe that these findings may guide the design of highly efficient noble metal catalysts to oxidate a broad range of biomass-derived alcohols for fuel cell applications.

Experimental

Synthesis of Ag@AgPd core–shell nanoplates

Typically, 64.5 mL of H_2O, 10 mL of polyvinylpyrrolidone (PVP, Mw 40 000, 5 wt%), 1.5 mL of NaOH (0.5 M), 1.5 mL of diethylamine, 2 mL of glucose (0.5 M), 20 mL of Ag nanoplates (edge length: ~35 nm, Ag: ~1.7 mM), and 0.2–0.6 mL of $NaPdCl_4$ (0.05 M) were added to a glass vial in sequence under vigorous stirring at 60 °C. After 6 h, Ag@AgPd core–shell nanoplates were collected by centrifugation, washed with H_2O, and redispersed in 2 mL of H_2O.

Electrochemical measurements

All electrochemical measurements were taken on a CHI 760e workstation. A rotating disk electrode (RDE), a Pt foil, and a saturated calomel electrode were used as the working, counter, and reference electrodes. The Ag@AgPd core–shell nanoplates were supported on Vulcan XC-72 carbon and dispersed in H_2O/isopropanol/nafion (5%) (1 : 1 : 0.004, volume ratio) to form a stable ink. Then, an aliquot of the ink containing 1 μg of Pd was dropped and dried on an RDE. CV curves were collected in N_2-saturated 1 M KOH + 1 M EtOH. The potential was scanned in the range of 0.135–1.235 V vs. the reversible hydrogen electrode (RHE) at a rate of 50 mV s^{-1} to evaluate the EOR activity.

Analysis of the C1- and C2-path faradaic efficiencies

The concentrations of the C2-path products (CH_3COOH and CH_3CHO) were measured by HPLC. Standard curves were first obtained by plotting HPLC peak areas against the concentrations. A chronoamperometric i–t test was then conducted at 0.635 V in N_2-saturated 0.1 M KOH + 1 M EtOH and stopped when the quantity of electricity reached 50 C. HPLC then

analyzed the electrolyte with the concentrations of CH_3COOH and CH_3CHO determined according to the standard curves. The FEs of the C2-path products can be calculated as FE = mnF/Q, where F is the Faraday constant, m is the quantity of the product (mol), and n is the number of transferred electrons ($n = 2$ for CH_3CHO; $n = 4$ for CH_3COOH). The FE of the C1-path reaction was calculated by subtracting the C2-path FE from 100% FE.

DFT calculation

The quantum mechanics (QM) calculations were carried out using VASP software, version 5.4.4.[52–55] We used the Perdew, Burke, and Ernzerhof (PBE) functional[56] of density functional theory (DFT) with the post-stage DFT-D3 method to correct for London dispersion (van der Waals attraction) with Becke–Johnson damping.[57] The projector augmented wave (PAW) method was used to account for core–valence interactions.[58] The kinetic energy cutoff for plane wave expansions was set to 400 eV, and the reciprocal space was sampled by using the Γ-centered Monkhorst–Pack scheme with a grid of 3 × 3 × 1. The vacuum layer is at least 15 Å above the surface. The convergence criteria are 1 × 10^{-5} eV energy differences for solving the electronic wave function. The Methfessel–Paxton smearing of second order with a width of 0.1 eV was applied. All geometries (atomic coordinates) were converged to within 3 × 10^{-2} eV Å^{-1} for maximal components of forces.

Characterization

TEM, HRTEM, and spherical-aberration-corrected HRTEM were performed on a Hitachi HT-7700, a JEM-F200-TEM, and a JEM-ARM300F (Grand), respectively. UV-vis spectra were obtained on an Ocean Optics HR2000+ES UV-vis-NIR spectrophotometer with a DH-2000-Bal light source. XRD patterns were recorded on a Rigaku SmartLab powder X-ray diffractometer equipped with Cu Kα radiation. XPS was performed on an ESCALAB Xi+ with monochromatic Al Kα radiation. Inductively coupled plasma mass spectrometry (ICP-MS) was performed on a PerkinElmer NexION 350D. HPLC analysis was performed on an Agilent 1260 LC liquid chromatography.

Conflicts of interest

There are no conflicts to declare.

Acknowledgements

References

1 E. Antolini, *J. Power Sources*, 2007, **170**, 1–12.

2 E. Antolini and E. R. Gonzalez, *J. Power Sources*, 2010, **195**, 3431–3450.

3 C. Bianchini and P. K. Shen, *Chem. Rev.*, 2009, **109**, 4183–4206.

4 W. Hong, J. Wang and E. Wang, *ACS Appl. Mater. Interfaces*, 2014, **6**, 9481–9487.

5 Z. X. Liang, T. S. Zhao, J. B. Xu and L. D. Zhu, *Electrochim. Acta*, 2009, **54**, 2203–2208.

6 Y.-Y. Yang, J. Ren, Q.-X. Li, Z.-Y. Zhou, S.-G. Sun and W.-B. Cai, *ACS Catal.*, 2014, **4**, 798–803.

7 X. Fang, L. Wang, P. K. Shen, G. Cui and C. Bianchini, *J. Power Sources*, 2010, **195**, 1375–1378.

8 Z.-Y. Zhou, Q. Wang, J.-L. Lin, N. Tian and S.-G. Sun, *Electrochim. Acta*, 2010, **55**, 7995–7999.

9 Y. Zhu, L. Bu, Q. Shao and X. Huang, *ACS Catal.*, 2020, **10**, 3455–3461.

10 Z. Liang, L. Song, S. Deng, Y. Zhu, E. Stavitski, R. R. Adzic, J. Chen and J. X. Wang, *J. Am. Chem. Soc.*, 2019, **141**, 9629–9636.

11 S.-H. Han, H.-M. Liu, P. Chen, J.-X. Jiang and Y. Chen, *Adv. Energy Mater.*, 2018, **8**, 1801326.

12 M. Li, D. A. Cullen, K. Sasaki, N. S. Marinkovic, K. More and R. R. Adzic, *J. Am. Chem. Soc.*, 2013, **135**, 132–141.

13 W. Wang, X. Zhang, Y. Zhang, X. Chen, J. Ye, J. Chen, Z. Lyu, X. Chen, Q. Kuang, S. Xie and Z. Xie, *Nano Lett.*, 2020, **20**, 5458–5464.

14 A. Kowal, M. Li, M. Shao, K. Sasaki, M. B. Vukmirovic, J. Zhang, N. S. Marinkovic, P. Liu, A. I. Frenkel and R. R. Adzic, *Nat. Mater.*, 2009, **8**, 325–330.

15 S. Bai, Y. Xu, K. Cao and X. Huang, *Adv. Mater.*, 2020, **33**, 2005767.

16 J. Ge, P. Wei, G. Wu, Y. Liu, T. Yuan, Z. Li, Y. Qu, Y. Wu, H. Li, Z. Zhuang, X. Hong and Y. Li, *Angew. Chem., Int. Ed.*, 2018, **57**, 3435–3438.

17 M. Z. F. Kamarudin, S. K. Kamarudin, M. S. Masdar and W. R. W. Daud, *Int. J. Hydrogen Energy*, 2013, **38**, 9438–9453.

18 Z. Chen, J. Zhang, Y. Zhang, Y. Liu, X. Han, C. Zhong, W. Hu and Y. Deng, *Nano Energy*, 2017, **42**, 353–362.

19 L. Zhang, Q. Chang, H. Chen and M. Shao, *Nano Energy*, 2016, **29**, 198–219.

20 Z. Xia and S. Guo, *Chem. Soc. Rev.*, 2019, **48**, 3265–3278.

21 L. Bu, N. Zhang, S. Guo, X. Zhang, J. Li, J. Yao, T. Wu, G. Lu, J.-Y. Ma, D. Su and X. Huang, *Science*, 2016, **354**, 1410–1414.

22 J. Wu, P. Li, Y.-T. F. Pan, S. Warren, X. Yin and H. Yang, *Chem. Soc. Rev.*, 2012, **41**, 8066–8069.

23 P. Strasser, S. Koh, T. Anniyev, J. Greeley, K. More, C. Yu, Z. Liu, S. Kaya, D. Nordlund, H. Ogasawara, M. F. Toney and A. Nilsson, *Nat. Chem.*, 2010, **2**, 454–460.

24 Y. Yao, X. K. Gu, D. He, Z. Li, W. Liu, Q. Xu, T. Yao, Y. Lin, H. J. Wang, C. Zhao, X. Wang, P. Yin, H. Li, X. Hong, S. Wei, W. X. Li, Y. Li and Y. Wu, *J. Am. Chem. Soc.*, 2019, **141**, 19964–19968.

25 X. Xia, Y. Wang, A. Ruditskiy and Y. Xia, *Adv. Mater.*, 2013, **25**, 6313–6333.

26 A. N. Chen, S. M. McClain, S. D. House, J. C. Yang and S. E. Skrabalak, *Chem. Mater.*, 2019, **31**, 1344–1351.

27 W. Wang, Z. Chen, Y. Shi, Z. Lyu, Z. Cao, H. Cheng, M. Chi, K. Xiao and Y. Xia, *ChemCatChem*, 2020, **12**, 5156–5163.

28 Z. Luo, J. Ahn and D. Qin, *Nanoscale*, 2019, **11**, 6710–6718.

29 L. Huang, J. Yang, M. Wu, Z. Shi, Z. Lin, X. Kang and S. Chen, *J. Power Sources*, 2018, **398**, 201–208.

30 J. Li, X. Sun and D. Qin, *ChemNanoMat*, 2016, **2**, 494–499.

31 J. Li, J. Liu, Y. Yang and D. Qin, *J. Am. Chem. Soc.*, 2015, **137**, 7039–7042.

32 A. Canlier, U. V. Ucak, H. Usta, C. Cho, J.-Y. Lee, U. Sen and M. Citir, *Appl. Surf. Sci.*, 2015, **350**, 79–86.

33 Y. Jiang, Y. Lu, D. Han, Q. Zhang and L. Niu, *Nanotechnology*, 2012, **23**, 105609.

34 K. Tedsree, T. Li, S. Jones, C. W. A. Chan, K. M. K. Yu, P. A. J. Bagot, E. A. Marquis, G. D. W. Smith and S. C. E. Tsang, *Nat. Nanotechnol.*, 2011, **6**, 302–307.

35 H. Liu, P. Zhong, K. Liu, L. Han, H. Zheng, Y. Yin and C. Gao, *Chem. Sci.*, 2018, **9**, 398–404.

36 H. Liu, K. Liu, P. Zhong, J. Qi, J. Bian, Q. Fan, K. Ren, H. Zheng, L. Han, Y. Yin and C. Gao, *Chem. Mater.*, 2018, **30**, 7744–7751.

37 H. Liu, T. Liu, L. Zhang, L. Han, C. Gao and Y. Yin, *Adv. Funct. Mater.*, 2015, **25**, 5435–5443.

38 C. Gao, Z. Lu, Y. Liu, Q. Zhang, M. Chi, Q. Cheng and Y. Yin, *Angew. Chem., Int. Ed.*, 2012, **51**, 5629–5633.

39 C. Xue, X. Chen, S. J. Hurst and C. A. Mirkin, *Adv. Mater.*, 2007, **19**, 4071–4074.

40 H. L. Skriver and N. M. Rosengaard, *Phys. Rev. B: Condens. Matter Mater. Phys.*, 1992, **46**, 7157–7168.

41 T. Song, F. Gao, L. Jin, Y. Zhang, C. Wang, S. Li, C. Chen and Y. Du, *J. Colloid Interface Sci.*, 2020, **560**, 802–810.

42 F. Zhao, C. Li, Q. Yuan, F. Yang, B. Luo, Z. Xie, X. Yang, Z. Zhou and X. Wang, *Nanoscale*, 2019, **11**, 19448–19454.

43 J. Guo, R. Huang, Y. Li, Z. Yu, L. Wan, L. Huang, B. Xu, J. Ye and S. Sun, *J. Phys. Chem. C*, 2019, **123**, 23554–23562.

44 M. Li, K. Duanmu, C. Wan, T. Cheng, L. Zhang, S. Dai, W. Chen, Z. Zhao, P. Li, H. Fei, Y. Zhu, R. Yu, J. Luo, K. Zang, Z. Lin, M. Ding, J. Huang, H. Sun, J. Guo, X. Pan, W. A. Goddard, P. Sautet, Y. Huang and X. Duan, *Nat. Catal.*, 2019, **2**, 495–503.

45 L. Chen, L. Lu, H. Zhu, Y. Chen, Y. Huang, Y. Li and L. Wang, *Nat. Commun.*, 2017, **8**, 14136.

46 J. W. Hong, Y. Kim, D. H. Wi, S. Lee, S.-U. Lee, Y. W. Lee, S.-I. Choi and S. W. Han, *Angew. Chem., Int. Ed.*, 2016, **55**, 2753–2758.

47 S. T. Nguyen, H. M. Law, H. T. Nguyen, N. Kristian, S. Wang, S. H. Chan and X. Wang, *Appl. Catal., B*, 2009, **91**, 507–515.

48 P. Strasser, S. Koh, T. Anniyev, J. Greeley, K. More, C. Yu, Z. Liu, S. Kaya, D. Nordlund, H. Ogasawara, M. F. Toney and A. Nilsson, *Nat. Chem.*, 2010, **2**, 454.

49 M. Mavrikakis, B. Hammer and J. K. Nørskov, *Phys. Rev. Lett.*, 1998, **81**, 2819–2822.

50 B. S. Mun, M. Watanabe, M. Rossi, V. Stamenkovic, N. M. Markovic and P. N. Ross Jr, *J. Chem. Phys.*, 2005, **123**, 204717.

51 P. Ferrin and M. Mavrikakis, *J. Am. Chem. Soc.*, 2009, **131**, 14381–14389.

52 G. Kresse and J. Hafner, *Phys. Rev. B: Condens. Matter Mater. Phys.*, 1993, **47**, 558–561.

53 G. Kresse and J. Furthmüller, *Comput. Mater. Sci.*, 1996, **6**, 15–50.

54 G. Kresse and J. Furthmüller, *Phys. Rev. B: Condens. Matter Mater. Phys.*, 1996, **54**, 11169–11186.

55 G. Kresse and J. Hafner, *Phys. Rev. B: Condens. Matter Mater. Phys.*, 1993, **47**, 558–561.

56 J. P. Perdew, K. Burke and M. Ernzerhof, *Phys. Rev. Lett.*, 1996, **77**, 3865–3868.

57 S. Grimme, J. Antony, S. Ehrlich and H. Krieg, *J. Chem. Phys.*, 2010, **132**, 154104.

58 G. Kresse and D. Joubert, *Phys. Rev. B: Condens. Matter Mater. Phys.*, 1999, **59**, 1758–1775.

15380 | *J. Mater. Chem. A*, 2021, **9**, 15373–15380

This journal is © The Royal Society of Chemistry 2021